# Leveraging Spatial Diversity for Ambiguity-Free Ultra-Narrowband Phase-Based 3D Localization

Guoyi Xu, *Student Member, IEEE*, and Edwin C. Kan, *Senior Member, IEEE*

***Abstract*—Phase-based 3D localization of radio-frequency (RF) markers has the advantage of high sensitivity and accuracy. However, phase measurements suffer from oscillator phase noises, wavelength ambiguities, and multi-path interferences. In the near field, antenna detuning and medium inhomogeneity render the phase-range relation nonlinear and non-monotonic, resulting in extra ambiguities and phase-center uncertainties, especially when the line-of-sight (LoS) path is obstructed. In this work, we present a novel framework for precision localization which leverages spatially diverse redundant channels to resolve ambiguities without relying on broad bandwidth. Spline-fitting was applied to selected reference locations, and measured differential phases were used to retrieve differential distances from curve fitting and to generate 3D location estimates. Ambiguities in phase, distances, and locations are resolved at various stages to identify ambiguity-free location from multiple candidates. An experimental multiple-input multiple-output (MIMO) network was implemented by Universal Software Radio Peripheral (USRP) devices and harmonic RF markers to demonstrate millimeter-level 3D localization at 900 MHz carrier frequency within a heavy multi-path ambient, simulating the condition inside building materials.**

***Index Terms*—phase ambiguity, phase-based localization, spatial diversity, ultra-narrowband.**

## I. INTRODUCTION

LOCALIZATION of radio-frequency (RF) markers plays a major role in the Internet of Things (IoT), as a critical sensing technology for a variety of applications including indoor navigation [1], [2], inventory tracking [3], [4], mapping [5], [6], robotic control [7]–[9], occupancy detection [10], [11], and structural monitoring [12], [13]. Conventionally the measuring device is situated in the far field from the target markers. The wireless channel is assumed to be Rician with ambient multi-paths regarded as unwanted interferences inside a predominantly homogeneous medium. Therefore, the plane-wave electromagnetic (EM) propagation and constant propagation speed establish the linear relation among traveling distance, traveling time, and carrier phase. Range-based trilateration then derives the 2D or 3D locations by two main approaches – continuous-wave (CW) carrier phase and wave-packet time of flight (ToF). Phase measurements suffer from inherent wavelength ambiguities and multi-path interferences, which can be resolved by broadband or multiple-frequency techniques to improve ranging accuracy [14]. Time-based localization can achieve high accuracy with short pulses [15] or frequency-modulated CW (FMCW) signals [16], but is strongly correlated with the bandwidth resources, which are heavily regulated and expensive [17]. Even with sufficient bandwidth, the high sampling rate poses further challenges to the hardware design as limited by the power budget [18].

Despite of numerous previous efforts, marker localization under the following constraints remains challenging due to ambiguities from: 1) near-field propagation; 2) inhomogeneous media; 3) heavy multi-path channels, especially with suppressed or blocked line-of-sight (LoS). For phase-based localization, phase-distance relations become nonlinear and non-monotonic with inhomogeneous media and blocked LoS in the near field [19], and can suffer more ambiguities. Phase centers of observation points, usually RF antennas, cannot be modeled by electrically small static points at their physical centers due to antenna detuning [20]. Tag localization inside building materials for structural integrity monitoring frequently encounters the above three constraints – To couple EM energy more effectively inside building materials such as concrete blocks, near field is preferred over far field; the signal path towards the embedded markers of interest is often deep inside inhomogeneous weight-bearing materials; supporting steel bars and brackets will create complex multi-path interferences.

In this paper, we propose a narrow-band CW phase-based 3D localization method enabled by spatial diversity without invoking far-field approximations. The major contributions of this work are:

1) The proposed localization resolves ambiguities arising from not only cyclic phase rotations but also nonlinear and non-monotonic phase-distance relations under near-field, complex media, and heavy multi-path conditions, enabling more realistic implementations.
2) Ambiguity was resolved by leveraging redundant channel information from spatially diverse observation points without relying on large bandwidth, which is advantageous for practical commercialization.
3) We verified the localization framework experimentally using a multiple-input multiple-output (MIMO) Universal Software Radio Peripheral (USRP) platform and harmonic radio-frequency identification (RFID) tags. The system achieved millimeter-level 3D localization accuracy in a near-field and heavy multi-path ambient, simulating the condition inside building materials.

The paper is organized as follows. Sec. II overviews the

This work was supported by the National Science Foundation (NSF) under Award CCSS 1945918. *(Corresponding author: Guoyi Xu).*

Guoyi Xu and Edwin C. Kan are with the School of Electrical and Computer Engineering, Cornell University, Ithaca, NY 14853 USA (e-mail: gx36@cornell.edu; eck5@cornell.edu).

related works on 3D localization methods using phase or ToF measurements with either frequency or spatial diversity. Sec. III introduces our localization method through a series of algorithms. Sec. IV presents the experimental validation, and Sec. V discusses insights, design considerations and future works. Sec. VI concludes this paper.

## II. Related Works

For the scope of this paper, we will limit our discussion to range-based localization, where ranging serves as the intermediate step preceding 3D localization.

*1) Far-Field Localization with Frequency Diversity*: Time-based approaches measure ToF or time-difference-of-arrival (TDoA) by transmitting an ultra-wideband (UWB) signal or FMCW chirp and receiving echoes from the target to extract accurate distance with low computational cost and improved robustness against multi-path [21], [22]. Researchers studied localization under non-line-of-sight (NLoS) conditions [23], [24], devised novel algorithms to identify NLoS over LoS [25], [26], or determined the optimal observation points in space to mitigate multi-path [27], [28]. Timing accuracy is correlated with bandwidth and resolution can be improved by a high sampling rate. Both factors directly affect the ranging accuracy, making such approaches highly susceptible to available spectrum resources and hardware limitations. In comparison, phase-based approaches measure the phase of CW signals received from the target and combine information over a continuous spectrum or multiple sparse frequencies to unravel wavelength ambiguity and retrieve range information. For example, SpotFi [29] and VWAN [30] exploited Wi-Fi subcarriers or multiple Wi-Fi bands to improve localization accuracy, and the heuristic multiple-frequency continuous-wave (HMFCW) was proposed to use multiple individual carrier frequencies with sufficient separation to resolve phase ambiguities and improve tolerance against large phase errors [14]. Similar to time-based approaches, a broad bandwidth is also needed for high localization accuracy.

*2) Far-Field Localization with Spatial Diversity*: When bandwidth is limited, another approach is spatial diversity. One commonly adopted technique is by deploying arrays of sensing points to synthesize a larger aperture than available from a single antenna [31], [32]. Array sensing also supports accurate azimuth selectivity using beam-steering, where angle-of-arrival (AoA) can be derived [33]–[35]. Another technique is through a multi-static sensor deployment for unambiguous reconstruction of the target location [36]–[38]. Combination of array processing and time-based ranging techniques have also been studied for accurate 3D localization, where both spatial and frequency diversity were exploited [22], [39]–[41].

*3) Near-Field Localization*: The phase-range relation can be nonlinear and non-monotonic in the near field [19], [42], and prior efforts improved localization by leveraging large antenna arrays and wavefront curvature [43], [44]. Compared to far-field approaches, near-field localization was less studied but has gained significant research interest due to its rich practical use cases and many open challenges.

Besides simulations and experimental validations, the literature has also seen abundant theoretical studies on localization performances, e.g., for fundamental limits on location estimation [45], [46], environmental-based optimal spatial and spectrum allocation [47], novel localization schemes in mm-wave [46], [48], and channel estimation [49].

## III. Localization Algorithms

The proposed 3D localization method consists of multiple stages: 1) spline fitting; 2) distance searching; 3) initial ambiguity removal; 4) voxel-tree location searching; 5) location ambiguity elimination. Differential phases are measured at all transmitter (Tx) and receiver (Rx) pairs for a small number of selected reference locations for calibration. For each Tx/Rx pair, an empirical relation between measured differential phases and known differential distances from the target to the Tx/Rx pair is defined by spline fitting. Next, differential phases for unknown locations are measured to search for differential distances from the spline curves, and multiple candidates exist for nonlinear and non-monotonic curves. An initial ambiguity removal algorithm removes least likely ones by leveraging spatial diversity. Then, a location searching algorithm generates a location contender set using distance candidates from a subset of all Tx/Rx pairs. Finally, a location ambiguity elimination algorithm identifies the most probable location out of location contender sets from different subsets of Tx/Rx pairs by exploiting spatial diversity from redundant channel resources.

### A. Pre-Processing and Spatial Diversity

The proposed localization framework is built upon phase measurements of all propagation channels between Tx and Rx. Simultaneously, each Tx transmits a CW signal modulated by in-phase and quadrature (I and Q) sinusoidal waveforms at a unique intermediate frequency (IF) for Tx separation, without baseband modulation. At each Rx, digital band-pass filters centered at each IF are applied to I and Q samples after demodulation, from which the carrier phase is calculated for each Tx [50]. As here Tx IF only serves for the multiplexing purpose, IF and their separations are purposefully set low to reduce the sampling rate requirement. Compared with GHz-level carrier frequency, the kHz-level bandwidth is much smaller than most existing localization methods. In this paper, we will show that the localization framework presents no dependence on bandwidth to resolve phase ambiguities.

Throughout the paper, unless otherwise noted, "phase" and "distance" refer to differential phase and differential distance

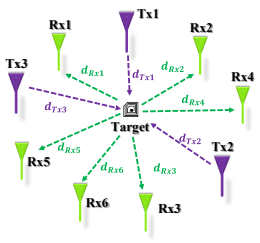


| Diff. Channel | Diff. Phase & Distance | Diff. Channel | Measured Param. |
|---|---|---|---|
| Tx12 | $\phi_{Tx12}, d_{Tx12}$ | Rx24 | $\phi_{Rx24}, d_{Rx24}$ |
| Tx13 | $\phi_{Tx13}, d_{Tx13}$ | Rx25 | $\phi_{Rx25}, d_{Rx25}$ |
| Tx23 | $\phi_{Tx23}, d_{Tx23}$ | Rx26 | $\phi_{Rx26}, d_{Rx26}$ |
| Rx12 | $\phi_{Rx12}, d_{Rx12}$ | Rx34 | $\phi_{Rx34}, d_{Rx34}$ |
| Rx13 | $\phi_{Rx13}, d_{Rx13}$ | Rx35 | $\phi_{Rx35}, d_{Rx35}$ |
| Rx14 | $\phi_{Rx14}, d_{Rx14}$ | Rx36 | $\phi_{Rx36}, d_{Rx36}$ |
| Rx15 | $\phi_{Rx15}, d_{Rx15}$ | Rx45 | $\phi_{Rx45}, d_{Rx45}$ |
| Rx16 | $\phi_{Rx16}, d_{Rx16}$ | Rx46 | $\phi_{Rx46}, d_{Rx46}$ |
| Rx23 | $\phi_{Rx23}, d_{Rx23}$ | Rx56 | $\phi_{Rx56}, d_{Rx56}$ |

Fig. 1. The schematics shows 3 Tx and 6 Rx antennas for localization, and the table lists all channels with corresponding phases and distances.

from a target to a Tx/Rx pair, respectively, and "channel" denotes one Tx/Rx pair, due to their extensive usage. Differential measurements enable an initial phase offset cancellation for channels with shared random initial phases of phase-locked loops (PLL) during frequency synthesis of local oscillators (LO) [51]. Then, calibration is required to obtain repeatable phase measurements for MIMO channels without shared LO. This is beyond the scope of this paper but will be briefly summarized in Sec. IV.D.

On the left, Fig. 1 shows the schematic of a MIMO network with 3 Tx and 6 Rx, where Tx antennas and downlink paths (from Tx antennas to the target) are marked in purple, and Rx antennas and uplink paths (from the target to Rx antennas) are marked in green. LoS from Tx to Rx and ambient multi-path are not shown. On the right, a table lists phases and distances in each channel, with 3 Tx pairs and 15 Rx pairs in total. In general, differential measurements add to the diversity compared with single Tx/Rx phase measurements, because the network with $M$ Tx and $N$ Rx consists of $Q = \frac{M(M-1)}{2} + \frac{N(N-1)}{2}$ differential pairs, which increases quadratically with the number of Tx/Rx. This provides abundant channel resources for 3D location searching, and the redundancy can be exploited to resolve location ambiguity.

In a MIMO network, baseband signals from each Tx to each Rx are retrieved. Specifically, the phase for Tx1 and Tx2 can be measured at each Rx, with IF1 and IF2 filtered out respectively. Likewise, the phase for Rx1 and Rx2 is available at each IF. For a network with $M$ Tx and $N$ Rx, totally there are $N \cdot \frac{M(M-1)}{2}$ and $M \cdot \frac{N(N-1)}{2}$ differential Tx and Rx measurements, respectively, which increase cubically with the number of Tx/Rx. Multiple measurements available from a single channel will be exploited for initial ambiguity removal.

### *B. Spline Fitting*

Unlike linear phase-distance relations in the far field and homogeneous media, a heavy multi-path channel in the near field is more complex [19]. Here, we explore the relation by curve fitting. The previous 3rd-order polynomial fitting and iterative fitting in [13] was time-consuming to obtain an optimized curve. Prolonged phase-distance relations in a large capture volume with complex multi-path have complicated curvature variations with more ambiguities. In addition, curve morphology varies over different channels, with some nearly linear and monotonic and others having many turnings and inflections. Without prior knowledge, the optimal polynomial fitting order is difficult to select for each channel, so segmented spline fitting was selected to mitigate local fitting errors.

Fig. 2 illustrates the complex phase-distance relations measured from experiments, and the accuracies of polynomial fitting with varying orders and 3rd-order spline fitting. Phase measurements and distance ground truths of reference locations are represented by red diamond markers. For spline fitting, these points are used as anchor points. Cyan circles represent ground truths for unknown locations, presented for evaluating fitting accuracy. Fig. 2(a) is an example when the phase-distance relation is nearly linear and monotonic over most of

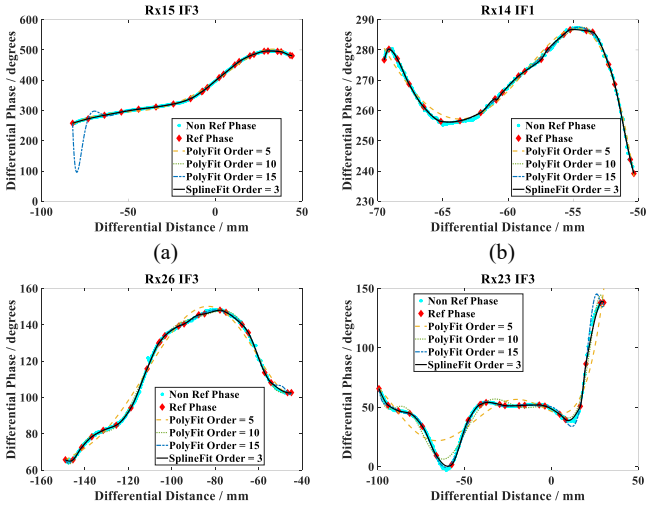


Fig. 2. (a)-(d) Curve fitting is applied to measured phases and distances of reference tag locations (red diamond markers). Fitted curves predict phases for non-reference tag locations as curves with different colors and shapes, with ground truths shown as cyan circles. Four representative channels are selected, and predictions are shown by the following fitting schemes: least-squares polynomial fitting with orders 5, 10 and 15, and 3rd-order least-squares spline fitting.

the curve, where polynomial fitting with orders 5 and 10 are both appropriate, but the order of 15 produces overshoots at the edge of the linear curve segment. Figs. 2(b) and (c) present two examples when the phase-distance relation contains non-monotonic segments while monotonic segments are more linear. There, polynomial fitting with orders 10 and 15 give good fitting but the order of 5 is insufficient for local variations especially near turning points. Fig. 2(d) shows an example when the phase-distance relation contains many large curvature variations over the entire curve. Polynomial fitting with orders 5 and 10 both exhibit inaccurate local fitting in some segments, while the order 15 produces overshoots elsewhere.

All examples show diverse variations of phase-distance relation curves, and hence the challenges in selecting an optimal and uniform polynomial order. In comparison, spline fitting has a superior performance than polynomial fitting of all selected orders, which minimizes the total least-squares error over the entire curve without ensuring good local fitting. Physically speaking, the phase-distance curves are continuous to the second-order derivatives, justifying the use of spline fitting.

### *C. Distance Searching*

Given the phase-distance curves from reference locations, the distance searching for unknown locations is then performed at each channel. Fig. 3 shows distance searching with given phase measurements of one unknown target location at four channels. Red diamond markers represent reference location, and values predicted by spline curves are shown in black. Cyan circles represent ground truths for target locations unknown in advance. Notice that for some channels, the same distance (but corresponding to two different physical locations) can give different phase measurements due to different multi-path interferences, with an example shown in Fig. 3(c). The constant-phase line can intersect with the phase-distance curve

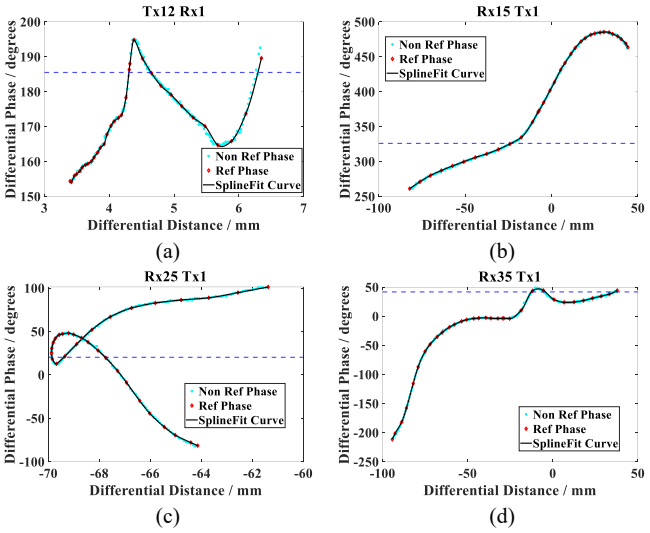


Fig. 3. (a)-(d) Four representative channels are shown with nonlinear and non-monotonic phase-distance relationships. All curves are fitted by 3rd-order least-squares splines curves, and each plot shows phases from ground truth non-reference location measurements (cyan circles), reference location measurements (red diamond markers) and spline fitting phase predictions (black lines).

at multiple points, each corresponding to a distance candidate, and the most challenging task is near the flat region, as the constant-phase line is almost tangential to the phase-distance curve to give a large distance error bound. To resolve this, we propose a recursive distance searching algorithm.

Fig. 4(a) shows curve intersections of one unknown location for one channel, with 164.39° measured phase. The distance range is divided into 1μm-resolution grid points, and we selected a heuristically pre-defined proportion (2% for this work) of those with best phase predictions as the coarse selection pool, shown by green square markers. Fig. 4(b) is a zoomed-in view for the right intersection in Fig. 4(a), enclosed in the orange dashed box, and the recursive distance searching (or fine selection) algorithm identifies two intersections. Fig. 4(c) shows the fine selection result for a measured phase of 164.21°, corresponding to another target location 1 mm away, and the intersection near the minimum is identified by recursive distance searching. For every coarse selection pool striding over a local extremum, the algorithm shrinks it by abandoning a pre-defined proportion of distance candidates (we selected 20% heuristically) with the worst phase predictions, and this process continues recursively until none of the new fine selection pools stride over a local extremum, shown as magenta triangle markers in Figs. 4(b) and (c). Physical centers of each fine selection pool are output as distance candidates. For Fig. 4(b), two fine selection pools are generated, centered at 5.71 mm and 5.77 mm, respectively. For Fig. 4(c), the candidate pool shrinks towards the local minimum around 5.73 mm. Without fine selection, these two cases cannot be distinguished given the similarity in their coarse selection pools. Fine selection provides sub-0.1mm distance error, which ensures high accuracy in further location searching as errors propagate and accumulate. The distance candidate corresponding to the left intersection in Fig. 4(a) is directly identified without fine selection, and ambiguities will be removed at later stages.

The distance searching algorithm is presented in Supplementary Algorithm I. The DBSCAN in Algorithm I stands for the density-based spatial clustering of applications with noise [52].

### *D. Initial Ambiguity Removal*

The MIMO communication scheme provides multiple phase-distance curves in each channel. Fig. 5(a) shows the example of phase-distance curves for the pair of Tx1 and Tx2, with different morphologies at Rx1 through Rx6. For an unknown location, the distance searching algorithm first determines the candidates for each curve, indicated by the intersection points with constant-phase lines in Fig. 5(a). Despite of the different candidate sets due to Rx spatial diversity, each curve contains one common candidate on the right, highlighted by magenta

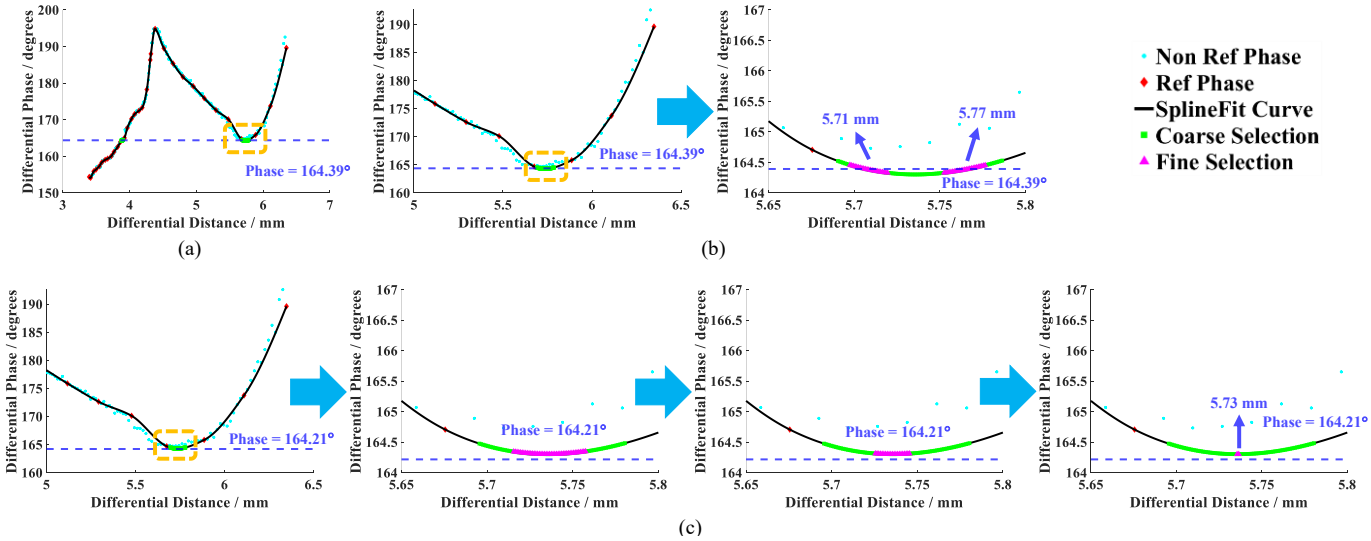


Fig. 4. (a) For an unknown tag location, with the measured phase of 164.39°, multiple differential distances are found by intersecting the horizontal constant-phase line with the phase-distance curve. (b) The right intersection, represented by the orange dashed box in (a), is located near its local minimum. Green square markers are distance candidates in the coarse selection pool, and magenta triangular markers are distance candidates after fine selection, identifying two separate distance candidates. (c) The intersection point of another constant-phase line of 164.21°, where fine selection identifies only one candidate.

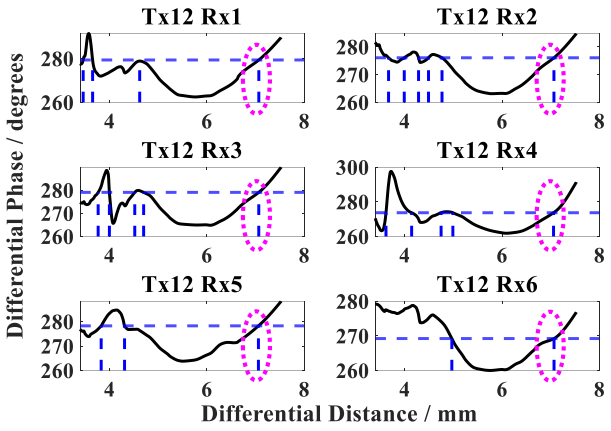


(a)

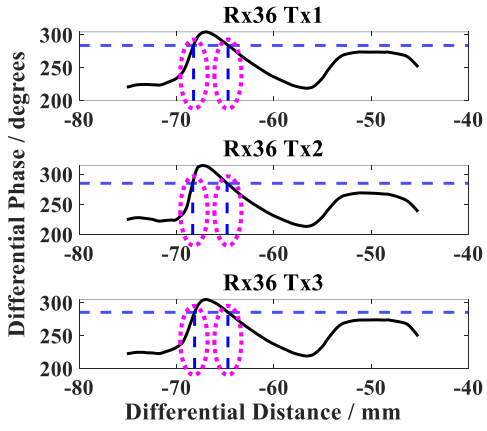


(b)

Fig. 5. Two examples of initial ambiguity removal. (a) Different curves from channel Tx12 measurements at each Rx give different distance candidate sets. The initial ambiguity removal algorithm identifies the common candidate and abandons all others before further processing, as shown in dashed magenta circles. (b) Differential measurements for channel Rx36 give two common distance candidates at each Tx, so no ambiguity is removed.

dashed circles. Because only one candidate corresponds to the ground truth, the common candidate present in all curves indicates that it is the correct one and all others are spurious. Fig. 5(b) shows another example of phase-distance curves for the pair of Rx3 and Rx6, where the curves for Tx1 to Tx3 are similar and give two common distance candidates. Hence, both candidates are likely correct and should be preserved for future steps. Therefore, the described routine does not guarantee complete ambiguity elimination but can serve as initial ambiguity removal to reduce computational burden at later steps of location searching and location ambiguity elimination. The initial ambiguity removal algorithm is performed for each channel, laid out in Supplementary Algorithm II.

### *E. Location Searching*

After distance searching and initial ambiguity removal for all channels, distance candidates are gathered to generate 3D locations, where the remaining distance ambiguities are converted to location ambiguities. Here, we present location searching for one set of unique distances from each channel and introduce location ambiguity elimination in Sec. II.F.

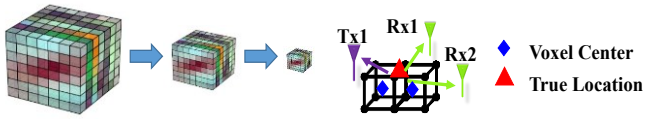


(a) (b)

Fig. 6. (a) The exponential capture volume reduction to reduce computational burden. (b) Visualization of insufficient voxel resolution for best-match location searching, justifying the use of more than one best-match locations during searching.

Given the distance for one channel, the 3D location is on the hyperbolic surface with constant differential distances from the foci, i.e., two Tx/Rx antennas. Therefore, it lies on the intersection of multiple hyperbolic surfaces corresponding to many channels. We implement a voxel-tree searching algorithm to find the 3D location, and Fig. 6(a) visualizes the voxel exponential reduction scheme. The algorithm is shown in Supplementary Algorithm III.

Compared with Algorithm I in [13], the major improvements in the location searching algorithm lies in selecting multiple location candidates rather than a single one with the best-matched differential distances for each channel. We occasionally observed inferior localization accuracy of the best-matched voxel compared with the 2nd- or 3rd-best-matched voxel. This was likely because the ground truth stood in between two neighboring voxels, or the distance candidates were inaccurate due to phase noise or degraded fitting. A visualization of insufficient voxel resolution is shown in Fig. 6(b). Moreover, the number of channels used to generate one 3D location, denoted by $P$ in Supplementary Algorithm III, can be increased with the abundant channel resources (in this work $P = 8$ while in [13] $P = 4$), to improve robustness and reduce sensitivity against distance errors from one particular channel.

### *F. Location Ambiguity Elimination*

With location ambiguities, a unique estimate for the target 3D location is needed. As mentioned before, a MIMO network with $M$ Tx and $N$ Rx has $Q = \frac{M(M-1)}{2} + \frac{N(N-1)}{2}$ channels. When $P$ channels are used to search for one location, totally $W = \binom{Q}{P} = \frac{Q(Q-1)(Q-2)\ldots(Q-P+1)}{P!}$ selections are available. Suppose all $Q$ channels have one unique distance candidate, the calculated 3D location should coincide under the perfect fitting condition regardless of $P$. With phase noise and fitting errors, calculated 3D locations from each subset of $P$ channels are slightly different but still within proximity. With ambiguities, each subset of $P$ channels generate a "location contender set", in which each location is generated from a combination of $P$ distance candidates of the subset using voxel-tree searching. Among the aggregate locations from all contender sets, spurious ones are scattered in space but correct ones are within close proximity, which can be found by spatial clustering.

Fig. 7(a) presents the flow chart for the ambiguity elimination algorithm, and Fig. 7(b) visualizes contender sets from different subsets of $P$ channels and clustering of the correct location candidates. The location ambiguity elimination algorithm is presented in Supplementary Algorithm IV.

Fig. 8 shows two examples of $J = 10$ contender sets, each

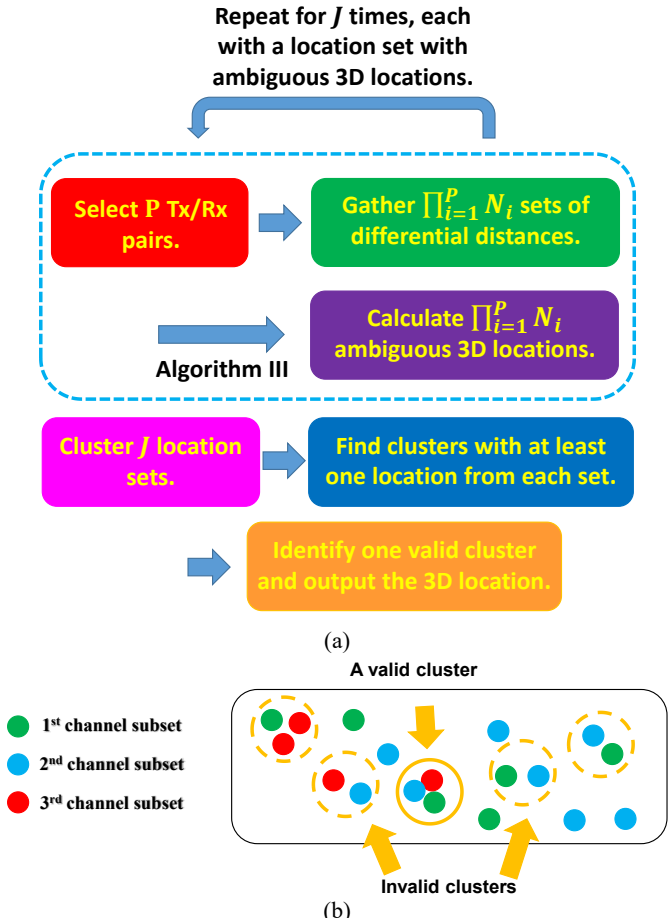


Fig. 7. (a) The ambiguity elimination algorithm, with more details in Algorithm IV. (b) Visualization of contender sets and spatial clustering.

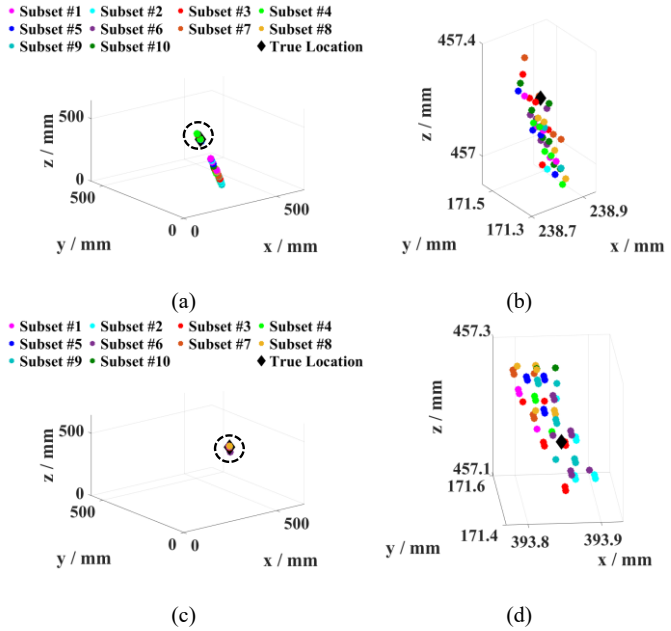


Fig. 8. (a) One experimental example of $J = 10$ contender sets, where $P = 8$ channels were selected for each set. Locations from each set are represented in a distinct color, and the black diamond marker represents the true tag location. The black dashed circle corresponds to the valid cluster determined by ambiguity elimination. (b) The zoomed-in view of the black dashed circle in (a). (c)-(d) Another experimental examples at a different non-reference tag location, with the same $J$ and $P$.

with $P = 8$ channels. In Fig. 8(a) each contender set is shown in an individual color, and within the black dashed circle is the valid cluster with at least one candidate from each contender set, corresponding to the correct target location. Spurious locations are outside the black dashed circle where no valid cluster can be found. Fig. 8(b) is a zoomed-in view of the black dashed circle in Fig. 8(a). Figs. 8(c) and (d) show another example where one single valid cluster is found, corresponding to the correct target location. The physical center of the identified valid cluster is taken as the final location estimate. For this work, $J$ and $P$ were empirically selected and kept constant throughout all experiments.

Furthermore, the described algorithm is revised to determine the wavelength integer and remove wavelength ambiguities due to cyclic phase rotations. As different channels have different wavelength numbers, only the true location with the correct wavelength integer appears in spatial proximity as a valid solution. The revised algorithm is shown in Supplementary Algorithm IV Variation.

## IV. Experimental Validation by a Prototype

### *A. Prototype Hardware Components*

We built an experimental prototype for the proposed localization using 3 National Instruments (NI) USRP Ettus B210 devices (Ettus Research, Austin, TX) and harmonic RFID tags. The prototype enables MIMO synchronized differential phase measurements after a phase calibration process.

Fig. 9(a) shows the Tx/Rx antenna placements, and Figs. 9(b) and (c) show top and side views of the prototype. The capture volume is enclosed within an aluminum frame of size 70 cm × 70 cm × 70 cm, constructed by bolt framing and fitting parts. Multiple concrete bricks filled the space within the capture volume to block the LoS of Tx/Rx antennas and create more multi-path propagations. Tx antennas transmitted signals backscattered by the harmonic RFID tag, which were received by Rx antennas. The tag was constructed by nonlinear transmission lines (NLTL) to generate the second harmonic carrier frequency [53], so that self-leakages, Tx-to-Rx LoS interferences, and downlink multi-path can be readily separated by Rx filtering. This also simplifies noise origin analysis at Tx and Rx. The tag was attached to a linear stepping motor, which has 1.25 μm resolution, and was configured to move in 1 mm steps over a total length of 300 mm. The driving track is made mostly of steel and aluminum causing even more complicated multi-path interferences. At each step the motor was stopped and phases for all channels were measured and saved.

We selected the Tx and Rx carrier frequencies as 900 MHz and 1.8 GHz, respectively, and the three IF used to modulate the carrier frequencies for Tx1 through Tx3 are 4 kHz, 12.5 kHz and 50 kHz, respectively. Therefore, after Rx demodulation, three IF components are located at 8 kHz, 25 kHz and 100 kHz, respectively, band-pass filtered in the digital domain with 100 Hz bandwidth centered at each IF to retrieve signals from each Tx. Figs. 9(d) and (e) show one Tx antenna (Abracon ARRKP7059-S915B with around 3.5 dBi gain at 900 MHz) and two Rx antennas (Siretta Delta 14 with around 1 dBi gain at 1.8

GHz), respectively. An NLTL harmonic tag is shown in Fig. 9(f). Fig. 9(g) shows one USRP B210 device and the global positioning system disciplined oscillator (GPSDO, BG7TBL 2018-06-05) used to provide a 10 MHz frequency reference and a 1 pulse per second (pps) baseband time reference for all 3 USRP devices. A schematic for the stepping motor is shown in Fig. 9(h). Both parallel displacement and tilt angle of the track installed on the stepping motor can be adjusted and we repeated the described linear stepping experiments over multiple trails.

### *B. Tag Localization Results*

Three stepping motor trails located at different regions of the capture volume and with different tilt angles were selected to present the localization results of the proposed framework. Fig. 10(a) shows the placements of Trails A to C, where Trails A and B are parallelly separated by 75 mm with horizontal placement, and Trail C is further separated from them with 4.5° tilt angle. Due to the multiple concrete bricks used for LoS blockage and multi-paths, there is limited space to deploy the linear module. However, 3D testing points were reasonably distributed in all dimensions.

The ground truth and estimated tag locations are plotted in Fig. 10(a) for each trail, where the estimated locations closely match ground truths along all the linear trails. Reference tag locations were selected for each trail for spline fitting. Distance searching and localization were applied for all other non-reference tag locations along the same trail. For this work, around 15% of locations were selected as reference locations. Ground truth for reference and non-reference tag locations are marked in yellow and red, respectively, and estimated tag locations are marked in blue. Figs. 10(b-d) present zoomed-in plots for the ground-truth and estimated tag 3D locations along Trails A through C, when the wavelength integer for any non-reference tag location was unknown. $N_{MaxWaveInt} = 1$ was selected in Supplementary Algorithm IV Variation, meaning that the correct wavelength integer was identified among -1, 0, and 1. It is worth noting that although prior knowledge of linear module length and capture volume size is required for selecting parameter $N_{MaxWaveInt}$, such knowledge usually can be easily obtained in practice. Fig. 10(e) shows the overall cumulative distribution function (CDF) of 3D localization errors for Figs. 10(b-d), where millimeter-level accuracy in 3D localization is achieved. This shows the effectiveness of the spatial diversity and redundant channels, as only 3 Tx and 6 Rx were used, a relatively small number in comparison with the antenna array approach [31].

### *C. Link Budget*

We performed link budget measurements for the prototype in Figs. 9(b)-(c), and the signal powers at various stages from Tx to Rx are shown in Fig. 11. As all Tx antennas are closely located, the tag received signal power and backscatter signal power have little variation, around 0 dBm and -18.3 dBm, respectively. However, diversity in Rx antenna location rendered large variation of received signal powers at each Rx, ranging from -73 dBm to -49 dBm. Potential improvements on the power loss can be from replacing the NLTL tag with a simpler nonlinear component such as a diode or rectenna, as the harmonic tag introduces 15-20 dB insertion loss by the NLTL structure [53]. As the proposed localization framework consumes negligible bandwidth, broadband operation by NLTL is not required.

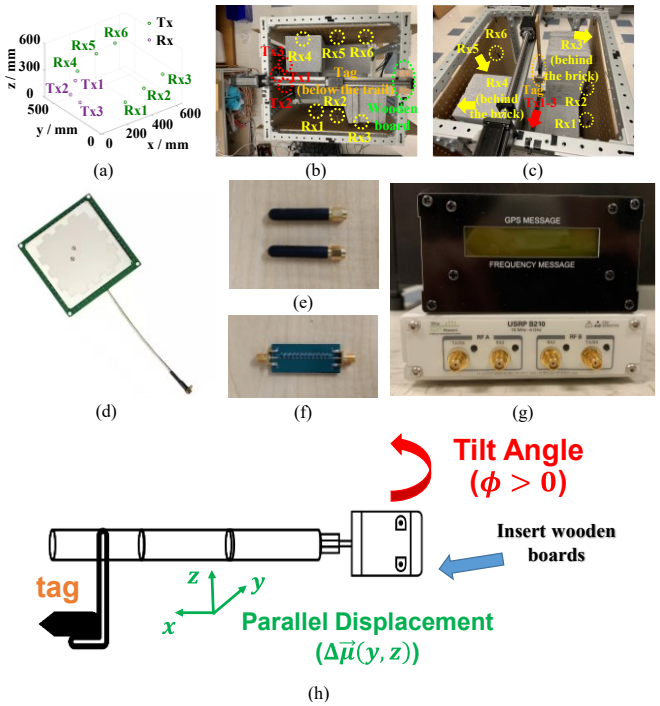


Fig. 9. (a) The Tx and Rx antenna placement for the experimental validation. (b)-(c) The top and side views of the experimental setup, where Tx, Rx antennas, the tag, and the stepping motor are shown. (d) A patch antenna operating around 900 MHz for Tx. (e) Whip antennas operating around 1.8 GHz for Rx. (f) A harmonic RFID tag. (g) The Universal Software Radio Peripheral (USRP) B210 device and global positioning system disciplined oscillator (GPSDO). (h) A schematic of the tag-carrying stepping motor with horizontal displacement. Tilt angle can be adjusted by inserting wood boards at one side.

Conventional non-harmonic backscattering tags with subcarrier uplink separation can also work, at the cost of higher phase noise close to the Tx carrier frequency.

### *D. MIMO Phase Synchronization*

Multistatic RF transceivers suffer from asynchronous phases among Tx/Rx channels and non-repeatable phases at each device startup, even with shared external frequency and time references [51]. This is due to the random LO initial phases by individual phase lock loops (PLLs) during frequency synthesis. Stringent requirements of individual PLLs to ensure synchronous phases [54] are not achievable in practice. To ensure repeatable phase measurements and synchronous phases, we directly measured the non-ideal random phase offsets using a known splitter-based wired channel and switched to the wireless channel to immediately remove it from measured phases. A detailed description of the phase calibration method would be published elsewhere due to length concerns.

## V. Discussions

### *A. Different Aspects of Spatial Diversity*

Spatial diversity is first exploited by initial ambiguity removal. Harmonic RFID decouples tag backscatter from Tx-to-Rx LoS, ambient interferences and self-leakages by different carrier frequencies, leading to similar Tx (Rx) differential phase-distance curves at each Rx (Tx) in the far field. However, in the near field, uncertainties in Tx/Rx antenna phase centers affect phase measurements, resulting in different phase-

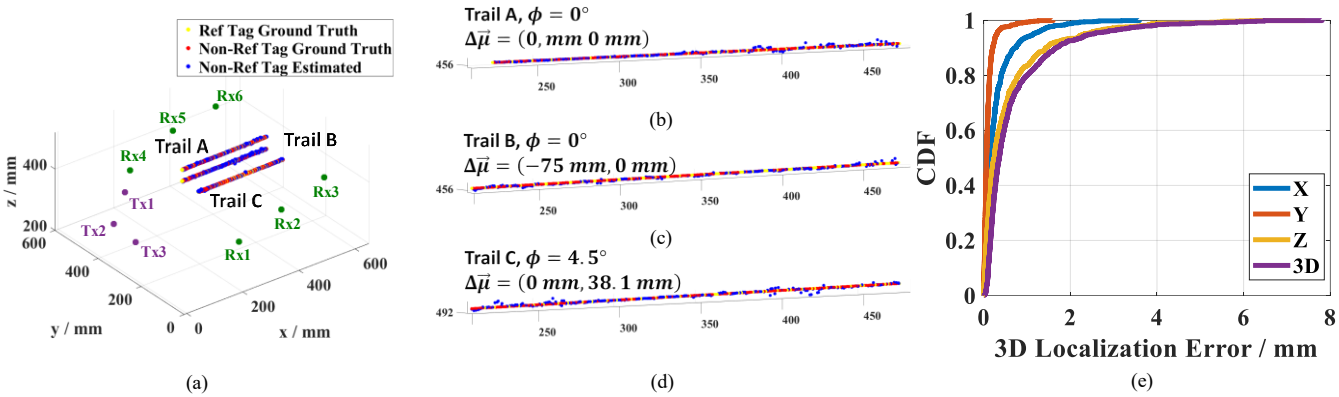


Fig. 10. (a) Tag localization results are shown along 3 stepping motor trails as blue markers, and the ground truth reference tag locations and non-reference tag locations are shown as yellow and red markers, respectively. (b)-(d) Zoomed-in views of localization results of Trails A-C shown in 10(a), with wavelength ambiguity elimination. (e) Overall cumulative distribution function (CDF) of 3D localization errors for the results in (b)-(d).

distance curves, which the initial ambiguity removal algorithm exploits to save computational resources for further steps. For non-harmonic/non-backscatter MIMO phase measurements, phase centers of Tx, Rx and target are dominant factors in the far field, while additional factors include uncertainties in Tx/Rx phase centers due to antenna detuning and multi-path in the near field, where different phase-distance curves can also be exploited.

Spatial diversity is exploited to a greater extent for ambiguity elimination. The large number of redundant channels provides much freedom to resolve the phase-distance ambiguity, because available Tx/Rx pairs are more than sufficient to generate a 3D location. In our experiments, sufficient spatial diversity in Tx/Rx antenna placement ensured the cluster corresponding to the correct target location can always be accurately identified.

### *B. Missing Detection vs. Ambiguous Detection*

While identifying the correct distance and location candidates among ambiguous ones requires extra effort, missing detection is much harder to cope with. Therefore, one major consideration is to ensure preference of generating ambiguity over missing detection. First, the example in Fig. 4(b) shows the recursive distance searching algorithm provides two closely located distance candidates near the local minimum, while the coarse selection cannot differentiate the two candidates and may lead to missing detection and large distance searching errors. Then, in location searching, we purposefully output all likely best-matched voxels rather than a single best-matched voxel, to tolerate 3D localization errors due to insufficient voxel resolution. Introduced ambiguities were finally resolved by spatial diversity. In comparison, if a distance candidate or location candidate is missing during any previous step, in no way can we retrieve it at later stages.

### *C. Reference Calibration*

The proposed localization framework requires selection of reference locations for unknown phase-distance relations. In our experiments, the selection was assisted with the phase-distance curve morphology observed from preliminary phase measurements. For a practical scenario such as structural monitoring, preliminary measurements are not available as RF markers are buried inside building materials, and the number of available reference points may be significantly reduced. Although we will not discuss these issues in full detail, we envision two main approaches to a more practical reference calibration. One approach is to perform reference calibration in another structure and transfer the data to the structure of interest, and the other approach is by modeling the structure and measuring the phase-distance relation through simulation.

### *D. Further Challenges and Future Work*

For future work, the proposed algorithm framework is expected to address the challenge of robustness against degraded fitting accuracy when phase measurements have reduced signal-to-noise ratio (SNR), or the proportion of reference locations is significantly reduced, e.g., from 15% down to 5%. In addition, the current channel subset selection is based only on subsets with fewest ambiguities, some without ambiguity at all. This can make location estimates biased towards channels with degraded fitting, while there may exist other channels with more accurate fitting but more ambiguities. Out of $W = \binom{Q}{P}$ selections of $P$ Tx/Rx pairs, there are $\binom{W}{J}$

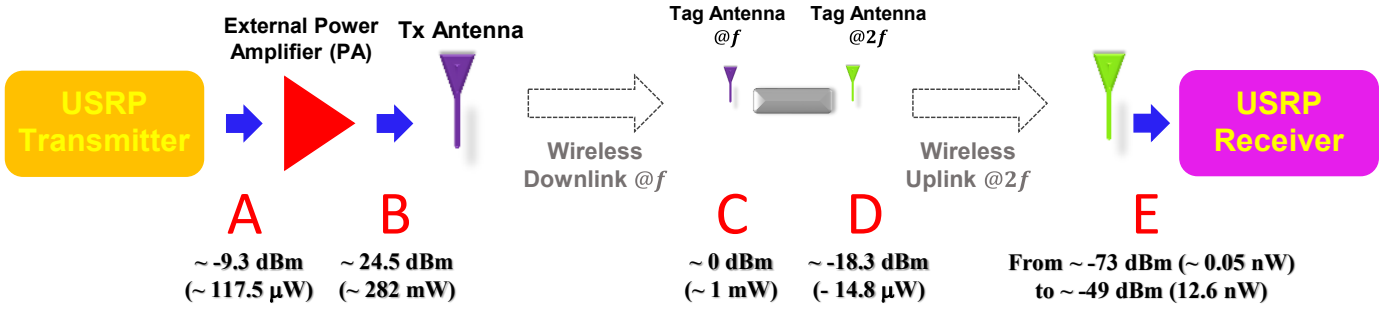


Fig. 11. Link budget analysis for the Tx-to-Rx channels, with varied Rx power depending on signal propagation distances.

different selections of $J$ Tx/Rx pairs, so optimizing the choice is usually impractical by exhaustive searching. Next, conditions for existence and uniqueness of the valid cluster corresponding to the ground truth can be studied. This can provide a better guidance on selecting number of Tx/Rx antennas and number of channels in a subset for ambiguity elimination. Finally, although the proposed 3D localization framework was demonstrated for phase-based localization in the near field, it can also be applied to far-field localization and time-based localization with bandwidth dependence. In the far field, phase-range and time-range relations can be linear, but ambiguities due to phase rotations can be resolved by our algorithm. For time-based localization with heavy multi-path interferences or inhomogeneous medium, potentially nonlinear or piecewise-linear time-range relations introduce ambiguities, which can also be similarly resolved. Different phase-range or time-range relations at multiple carrier frequencies over a wide bandwidth can also be combined to resolve ambiguity at an initial stage, together with the spatial diversity.

## VI. Conclusion

In this paper, we introduce a novel narrow-band framework for phase-based precision localization. Differential distances are retrieved from measured differential phases of multiple channels and are further combined to generate 3D locations. Ambiguities are resolved by leveraging redundant channel resources from spatially diverse Tx/Rx antennas, without relying on costly bandwidth resources. The proposed 3D localization framework was demonstrated by a prototype implemented by a USRP platform and harmonic RFID, showing millimeter-level 3D localization accuracy. The system worked under the conditions of near-field propagation and heavy multi-path environments with blocked LoS, and it also can be potentially applied to both phase-based and time-based localization setups with far-field assumptions and bandwidth dependence. Future works will focus on robustness against fitting accuracy, optimized channel subset selection, and theoretical studies of valid cluster existence and uniqueness.

## References

[1] Q. Zou, Q. Sun, L. Chen, B. Nie, and Q. Li, "A comparative analysis of LiDAR SLAM-based indoor navigation for autonomous vehicles," *IEEE Trans. Intell. Transp. Syst.*, vol. 23, no. 7, pp. 6907–6921, Jul. 2022, doi: 10.1109/TITS.2021.3063477.

[2] F. Jamil, N. Iqbal, S. Ahmad, and D.-H. Kim, "Toward accurate position estimation using learning to prediction algorithm in indoor navigation," *Sensors*, vol. 20, Art. no. 16, Jan. 2020, doi: 10.3390/s20164410.

[3] F. Jamil, N. Iqbal, S. Ahmad, and D.-H. Kim, "Toward accurate position estimation using learning to prediction algorithm in indoor navigation," *Sensors*, vol. 20, Art. no. 16, Jan. 2020, doi: 10.3390/s20164410.

[4] J. R. Parvin and C. Vasanthanayaki, "Particle swarm optimization-based energy efficient target tracking in wireless sensor network," *Measurement*, vol. 147, Art. no. 106882, Dec. 2019, doi: 10.1016/j.measurement.2019.106882.

[5] C. X. Lu *et al.*, "See through smoke: robust indoor mapping with low-cost mmWave radar," *Proc. the 18th Intl. Conf. Mobile Systems, Applications, and Services*, Toronto, ON, Canada, Jun. 2020, doi: 10.1145/3386901.3388945.

[6] S. Karam, F. Nex, B. T. Chidura, and N. Kerle, "Microdrone-based indoor mapping with graph SLAM," *Drones*, vol. 6, Art. no. 11, Nov. 2022, doi: 10.3390/drones6110352.

[7] M. Klingensmith, S. S. Sirinivasa, and M. Kaess, "Articulated robot motion for simultaneous localization and mapping (ARM-SLAM)," *IEEE Robot. Autom. Lett.,* vol. 1, no. 2, pp. 1156-1163, Jan. 2016, doi: 10.1109/LRA.2016.2518242.

[8] S. S. Vedaei and K. A. Wahid, "A localization method for wireless capsule endoscopy using side wall cameras and IMU sensor," *Sci. Rep.*, vol. 11, Art. no. 1, May 2021, doi: 10.1038/s41598-021-90523-w.

[9] A. S. Aguiar, F. N. dos Santos, J. B. Cunha, H. Sobreira, and A. J. Sousa, "Localization and mapping for robots in agriculture and forestry: a survey," *Robotics*, vol. 9, Art. no. 4, Dec. 2020, doi: 10.3390/robotics9040097.

[10] X. Tang and S. Mandal, "Indoor occupancy awareness and localization using passive electric field sensing," *IEEE Trans. Instrum. Meas.*, vol. 68, no. 11, pp. 4535–4549, Nov. 2019, doi: 10.1109/TIM.2018.2890319.

[11] P. Sharma, G. Xu, X. Hui, D. L. Hysell, and E. C. Kan, "Deep-learning-based occupant counting by ambient RF sensing," *IEEE Sens. J.*, vol. 21, no. 6, pp. 8564–8574, Mar. 2021, doi: 10.1109/JSEN.2020.3045035.

[12] A. B. Noel, A. Abdaoui, T. Elfouly, M. H. Ahmed, A. Badawy, and M. S. Shehata, "Structural Health Monitoring Using Wireless Sensor Networks: A Comprehensive Survey," *IEEE Commun. Surv. Tutor.,* doi: 10.1109/COMST.2017.2691551.

[13] G. Xu and E. C. Kan, "Ambiguity-free 3D millimeter-precision RFID tag localization inside building materials," *2023 IEEE Intl. Conf. RFID,* Seattle, WA, USA, Jun. 13-15, 2023.

[14] Y. Ma and E. C. Kan, "Accurate indoor ranging by broadband harmonic generation in passive NLTL backscatter tags," *IEEE Trans. Microw. Theory Tech.*, vol. 62, no. 5, pp. 1249–1261, May 2014, doi: 10.1109/TMTT.2014.2311381.

[15] R. Niu, R. S. Blum, P. K. Varshney, and A. L. Drozd, "Target localization and tracking in noncoherent multiple-input multiple-output radar systems," *IEEE Trans. Aerosp. Electron. Syst.,* vol. 48, no. 2, pp. 1466-1489, Apr. 2012, doi: 10.1109/TAES.2012.6178073.

[16] Z. Peng *et al.*, "A portable FMCW interferometry radar with programmable low-IF architecture for localization, ISAR imaging, and vital sign tracking," *IEEE Trans. Microw. Theory Tech.*, vol. 65, no. 4, pp. 1334–1344, Apr. 2017, doi: 10.1109/TMTT.2016.2633352.

[17] National Telecommunications and Information Administration. (2016, Jan.) *United States Frequency Allocation Chart.* [Online]. Available: https://ntia.gov/page/united-states-frequency-allocation-chart.

[18] F. Zafari, A. Gkelias, and K. K. Leung, "A survey of indoor localization systems and technologies," *IEEE Commun. Surv. Tutor.*, vol. 21, no. 3, pp. 2568–2599, Apr. 2019, doi: 10.1109/COMST.2019.2911558.

[19] B. Friedlander, "Localization of signals in the near-field of an antenna array," *IEEE Trans. Signal Process.*, vol. 67, no. 15, pp. 3885–3893, Aug. 2019, doi: 10.1109/TSP.2019.2923164.

[20] Y. Ma, H. Liu, Y. Zhang, and Y. Jiang, "The influence of the nonideal phase offset on SAR-based localization in passive UHF RFID," *IEEE Trans. Antennas Propag.*, vol. 68, no. 8, pp. 6346–6354, Aug. 2020, doi: 10.1109/TAP.2020.2982448.

[21] P. Wu, S. Su, Z. Zuo, X. Guo, B. Sun, and X. Wen, "Time difference of arrival (TDoA) localization combining weighted least squares and firefly algorithm," *Sensors*, vol. 19, Art. no. 11, Jan. 2019, doi: 10.3390/s19112554.

[22] K. Han and S. Hong, "Vocal signal detection and speaking-human localization with MIMO FMCW radar," *IEEE Trans. Microw. Theory Tech.*, vol. 69, no. 11, pp. 4791–4802, Nov. 2021, doi: 10.1109/TMTT.2021.3102233.

[23] M. Yang, D. R. Jackson, J. Chen, Z. Xiong, and J. T. Williams, "A TDOA localization method for nonline-of-sight scenarios," *IEEE Trans. Antennas Propag.*, vol. 67, no. 4, pp. 2666–2676, Apr. 2019, doi: 10.1109/TAP.2019.2891403.

[24] X. Zhang, L. Chen, M. Feng, and T. Jiang, "Toward reliable non-line-of-sight localization using multipath reflections," *Proc. ACM Interact. Mob. Wearable Ubiquitous Technol.*, Mar. 2022, doi: 10.1145/3517244.

[25] B. C. Tedeschini, M. Nicoli, and M. Z. Win, "On the latent space of mmWave MIMO channels for NLOS identification in 5G-advanced systems," *IEEE J. Sel. Areas Commun.*, vol. 41, no. 6, pp. 1655–1669, Jun. 2023, doi: 10.1109/JSAC.2023.3273769.

[26] C. Wu, H. Hou, W. Wang, Q. Huang, and X. Gao, "TDOA based indoor positioning with NLOS identification by machine learning," *2018 10th Intl. Conf. Wireless Communications and Signal Processing (WCSP)*, Hangzhou, China, Oct. 18-20, 2018, doi: 10.1109/WCSP.2018.8555654.

[27] W. Zhao, A. Goudar, and A. P. Schoellig, "Finding the right place: sensor placement for UWB time difference of arrival localization in cluttered indoor environments," *IEEE Robot. Autom. Lett.*, vol. 7, no. 3, pp. 6075–6082, Jul. 2022, doi: 10.1109/LRA.2022.3165181.
[28] Y. Zhao, N. Cheng, Z. Li, and B. Hao, "An efficient sensor selection algorithm for TDOA localization with estimated source position," *ICC 2022 - IEEE Intl. Conf. Communications*, Seoul, Korea, May 16-20, 2022, doi: 10.1109/ICC45855.2022.9838504.
[29] M. Kotaru, K. Joshi, D. Bharadia, and S. Katti, "SpotFi: Decimeter level localization using WiFi," *ACM SIGCOMM Comput. Commun. Rev.*, vol. 45, no. 4, pp. 269–282, Aug. 2015, doi: 10.1145/2829988.2787487.
[30] L. N. Kandel and S. Yu, "VWAN: Virtual WiFi ANtennas for Increased Indoor Localization Accuracy," *2019 IEEE Intl. Conf. Industrial Internet (ICII),* Orlando, FL, USA, Nov. 11-12, 2019, doi: 10.1109/ICII.2019.00052.
[31] F. Guidi, A. Guerra, and D. Dardari, "Personal mobile radars with millimeter-wave massive arrays for indoor mapping," *IEEE Trans. Mob. Comput.*, vol. 15, no. 6, pp. 1471–1484, Jun. 2016, doi: 10.1109/TMC.2015.2467373.
[32] B. Heiles *et al.*, "Ultrafast 3D ultrasound localization microscopy using a 32 × 32 matrix array," *IEEE Trans. Med. Imaging*, vol. 38, no. 9, pp. 2005–2015, Sep. 2019, doi: 10.1109/TMI.2018.2890358.
[33] R. Schmidt, "Multiple emitter location and signal parameter estimation," *IEEE Trans. Antennas Propag.*, vol. 34, no. 3, pp. 276–280, Mar. 1986, doi: 10.1109/TAP.1986.1143830.
[34] N. BniLam, D. Joosens, M. Aernouts, J. Steckel, and M. Weyn, "LoRay: AoA estimation system for long range communication networks," *IEEE Trans. Wirel. Commun.*, vol. 20, no. 3, pp. 2005–2018, Mar. 2021, doi: 10.1109/TWC.2020.3038565.
[35] G. Avitabile, A. Florio, and G. Coviello, "Angle of arrival estimation through a full-hardware approach for adaptive beamforming," *IEEE Trans. Circuits Syst. II Express Briefs*, vol. 67, no. 12, pp. 3033–3037, Dec. 2020, doi: 10.1109/TCSII.2020.2995064.
[36] D. L. Hysell, P. Sharma, M. Urco, and M. A. Milla, "Aperture-synthesis radar imaging with compressive sensing for ionospheric research," *Radio Sci.*, vol. 54, no. 6, pp. 503–516, 2019, doi: 10.1029/2019RS006805.
[37] G. Xu, P. Sharma, X. Hui, and E. C. Kan, "3-D indoor device-free object detection by passive radio frequency identification," *IEEE Trans. Instrum. Meas.*, vol. 70, pp. 1–13, 2021, doi: 10.1109/TIM.2021.3059309.
[38] G. Xu, P. Sharma, D. L. Hysell, and E. C. Kan, "Indoor object sensing using radio-frequency identification with inverse methods," *IEEE Sens. J.*, vol. 22, no. 12, pp. 11336–11344, Jun. 2022, doi: 10.1109/JSEN.2021.3086700.
[39] J.-K. Park, J.-H. Park, and K.-T. Kim, "Multipath signal mitigation for indoor localization based on MIMO FMCW radar system," *IEEE Internet Things J.*, pp. 1–1, 2023, doi: 10.1109/JIOT.2023.3292349.
[40] M. Aernouts, N. BniLam, R. Berkvens, and M. Weyn, "TDAoA: A combination of TDoA and AoA localization with LoRaWAN," *Internet Things*, vol. 11, p. 100236, Sep. 2020, doi: 10.1016/j.iot.2020.100236.
[41] M. Wu and C. Hao, "Super-resolution TOA and AOA estimation for OFDM radar systems based on compressed sensing," *IEEE Trans. Aerosp. Electron. Syst.*, vol. 58, no. 6, pp. 5730–5740, Dec. 2022, doi: 10.1109/TAES.2022.3178393.
[42] E. Joy and D. Paris, "Spatial sampling and filtering in near-field measurements," *IEEE Trans. Antennas Propag.*, vol. 20, no. 3, pp. 253–261, May 1972, doi: 10.1109/TAP.1972.1140193.
[43] Z. Abu-Shaban, K. Keykhosravi, M. F. Keskin, G. C. Alexandropoulos, G. Seco-Granados, and H. Wymeersch, "Near-field localization with a reconfigurable intelligent surface acting as lens," *ICC 2021 - IEEE Intl. Conf. Communications*, Montreal, QC, Canada, Jun. 14-23, 2021, doi: 10.1109/ICC42927.2021.9500663.
[44] Z. Zheng, M. Fu, W.-Q. Wang, S. Zhang, and Y. Liao, "Localization of mixed near-field and far-field sources using symmetric double-nested arrays," *IEEE Trans. Antennas Propag.*, vol. 67, no. 11, pp. 7059–7070, Nov. 2019, doi: 10.1109/TAP.2019.2925199.
[45] C. Tian, Y. Ma, X. Liang, W. Ning, and H. Zhao, "On absoluteness and stationary condition of WMDS for range-based localization," *IEEE Internet Things J.*, vol. 10, no. 11, pp. 10066–10079, Jun. 2023, doi: 10.1109/JIOT.2023.3236427.
[46] J. He, A. Fakhreddine, and G. C. Alexandropoulos, "Simultaneous indoor and outdoor 3D localization with STAR-RIS-assisted millimeter wave systems," *2022 IEEE 96th Vehicular Technology Conf. (VTC2022-Fall)*, London, United Kingdom, Sep. 26-29, 2022, doi: 10.1109/VTC2022-Fall57202.2022.10013055.
[47] Y. Long, Y. Zeng, X. Xu, and Y. Huang, "Environment-aware wireless localization enabled by channel knowledge map," *GLOBECOM 2022 - 2022 IEEE Global Communications Conf.*, Rio de Janeiro, Brazil, Dec. 4-8, 2022, doi: 10.1109/GLOBECOM48099.2022.10001045.
[48] S. Hu, F. Rusek, and O. Edfors, "Beyond massive MIMO: the potential of positioning with large intelligent surfaces," *IEEE Trans. Signal Process.*, vol. 66, no. 7, pp. 1761–1774, Apr. 2018, doi: 10.1109/TSP.2018.2795547.
[49] M. Cui and L. Dai, "Channel estimation for extremely large-scale MIMO: far-field or near-field?" *IEEE Trans. Commun.*, vol. 70, no. 4, pp. 2663–2677, Apr. 2022, doi: 10.1109/TCOMM.2022.3146400.
[50] J. Zhou, T. B. Conroy, G. Xu, and E. C. Kan, "Morphology transformation and content selection of near-field RF sensing by complex vector injection," *IEEE J. Electromagn. RF Microw. Med. Biol.*, vol. 6, no. 4, pp. 555–565, Dec. 2022, doi: 10.1109/JERM.2022.3199615.
[51] Y. Zhang *et al.*, "Removing random phase contributions of sweeping local oscillator from modulated RF measurements," *IEEE Trans. Microw. Theory Tech.*, vol. 66, no. 12, pp. 5737–5749, Dec. 2018, doi: 10.1109/TMTT.2018.2879507.
[52] M. Ester, H.-P. Kriegel, J. Sander, and X. Xu, "A density-based algorithm for discovering clusters in large spatial databases with noise," *Proc. the Second Intl. Conf. Knowledge Discovery and Data Mining*, Portland, Oregon, USA, Aug. 1996, doi: 10.5555/3001460.3001507.
[53] F. Yu, K. G. Lyon, and E. C. Kan, "A novel passive RFID transponder using harmonic generation of nonlinear transmission lines," *IEEE Trans. Microw. Theory Tech.*, vol. 58, no. 12, pp. 4121–4127, Dec. 2010, doi: 10.1109/TMTT.2010.2088134.
[54] T. Harzheim and H. Heuermann, "Phase repeatable synthesizers as a new harmonic phase standard for nonlinear network analysis," *IEEE Trans. Microw. Theory Tech.*, vol. 66, no. 6, pp. 2888–2895, Jun. 2018, doi: 10.1109/TMTT.2018.2817513.

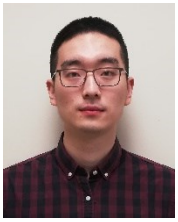

**Guoyi Xu** (Graduate Student Member, IEEE) received a B.Eng. degree in Electrical Engineering from the University of Electronic Science and Technology of China (UESTC), Chengdu, China, in 2018, and the Ph.D. degree in Electrical and Computer Engineering from Cornell University, Ithaca, NY, USA, in 2023. He is currently working as a postdoctoral researcher scientist in the department Electrical Engineering at Columbia University, New York, NY, USA. His research interests include RF systems, RFID, RFIC, and IoT.

**Edwin C. Kan** (Senior Member, IEEE) received a B.S. degree from National Taiwan University in 1984, and M.S. and Ph.D. degrees from the University of Illinois, Urbana-Champaign in 1988 and 1992, respectively, all in Electrical Engineering. In January 1992, he joined Dawn Technologies, Sunnyvale CA, as a CAD Engineer. He was then with Stanford University as a Research Associate from 1994 to 1997. In 1997, he started as an Assistant Professor in School of Electrical and Computer Engineering, Cornell University, Ithaca, NY, where he is now a professor. His research interests include RF biosensors, RFID, RF imaging, CMOS technology, Flash memory, molecular sensors, and technology computer-aided design (TCAD).